

Water exchange and microscopic kurtosis – two sides of the same coin?

Arthur Chakwizira¹, Filip Szczepankiewicz¹, and Markus Nilsson²

1. Medical Radiation Physics, Clinical Sciences Lund, Lund University, Lund, Sweden
2. Department of Clinical Sciences Lund, Radiology, Lund University, Lund, Sweden

Corresponding author:

Arthur Chakwizira

Department of Medical Radiation Physics, Lund University, Skåne University Hospital,
SE-22185 Lund, Sweden

Email address: arthur.chakwizira@med.lu.se

Word count: 6500

Sponsors/Grant numbers:

- VR (Swedish Research Council)
 - 2020-04549
 - 2021-04844
- eSENCE
 - 10:5
- Cancerfonden (The Swedish Cancer Society)
 - 2022/2414
 - 22 0592 JIA

Keywords:

Diffusion MRI, time dependence, double diffusion encoding, restricted diffusion, exchange, microscopic kurtosis, correlation tensor imaging, intra-compartmental kurtosis

Abstract

Diffusion MRI is sensitive to a wide range of features of the microstructure including diffusivity, exchange and three sources of diffusional kurtosis: isotropic, anisotropic, and microscopic. Correlation tensor imaging (CTI) uses double diffusion encoding (DDE) to resolve all three kurtosis components. In that framework, microscopic kurtosis is estimated from the contrast between SDE and parallel DDE signals at the same b-value. Another approach is multi-Gaussian exchange (MGE), which can apply DDE to measure exchange. The highest exchange sensitivity in MGE is obtained by contrasting SDE and DDE signals at the same b-value. CTI and MGE can thus be applied to analyse the same data, but exchange can bias microscopic kurtosis estimates if not accounted for, and vice versa. Here, we develop new theory (MGE incorporating microscopic kurtosis, μ MGE) that accounts for both effects, by exploiting the distinct signatures of exchange and microscopic kurtosis with varying mixing time: exchange causes a dependence of the signal on mixing time while microscopic kurtosis does not. We perform Monte-Carlo simulations in different geometries with varying levels of exchange and study the behaviour of the parameters from CTI, MGE, and μ MGE. We conclude that microscopic kurtosis from CTI is positively biased by exchange. We also find that applying μ MGE to data acquired with multiple mixing times for both parallel and orthogonal DDE allows accurate estimation of exchange and all three sources of kurtosis.

1 Introduction

Diffusion magnetic resonance imaging (dMRI) is a powerful radiological tool due to both its non-invasive nature and its exquisite sensitivity to the microstructure of biological tissue (Le Bihan 2014; Nilsson et al. 2018; Alexander et al. 2019). It provides a significant contribution to radiology, for example, by enabling measurements of the apparent diffusion coefficient (ADC). The utility of the ADC is its high sensitivity to microstructural tissue changes (Moseley et al. 1990b; Albers 1999; Chenevert et al. 2000; Ross et al. 2003; Tsien et al. 2014; Drake-Pérez et al. 2018). However, it is not very specific because it responds to multiple aspects of tissue microstructure (Reynaud 2017; Brabec et al. 2023; Lampinen et al. 2023). A key reason for the poor specificity of the ADC, and dMRI in

general, is the experimental design on which most dMRI applications rely: the so-called single diffusion encoding (SDE) scheme proposed in 1965 by Stejskal and Tanner (Stejskal and Tanner 1965) and later designated this name by (Shemesh et al. 2016). Although widely used for a variety of purposes (Callaghan et al. 1988; Moseley et al. 1990b, 1990a; Basser et al. 1994; Jensen et al. 2005; Assaf et al. 2008; Fieremans et al. 2011, 2016; Chen et al. 2012; Özarslan et al. 2013; Panagiotaki et al. 2014; Chuhutin et al. 2017; Aggarwal et al. 2020; Lee et al. 2020; Zhang et al. 2021), SDE is a poor probe of heterogenous tissue because it conflates several microstructural features such as microscopic diffusion anisotropy, orientation dispersion and isotropic heterogeneity (Özarslan and Basser 2008; Szczepankiewicz et al. 2015; Westin et al. 2016). To address the shortcomings of SDE, the double diffusion encoding (DDE) scheme, which uses two pairs of diffusion-sensitising pulses separated by a mixing time was introduced in a pioneering study in 1990 (Cory et al. 1990). That study showed that DDE acquisitions with parallel and orthogonal gradient pairs enabled measurement of the local eccentricity of a sample, even when the sample appeared isotropic at the voxel scale due to orientation dispersion. It was later shown that additional specificity can be gained by DDE in other scenarios too, for example, to separate microscopic anisotropy from orientation dispersion (Callaghan and Komlosh 2002; Özarslan and Basser 2008; Shemesh et al. 2010; Jespersen et al. 2013), measure flow (Caprihan and Fukushima 1990; Callaghan and Xia 1991), estimate pore sizes (Mitra 1995; Koch and Finsterbusch 2011), probe microscopic kurtosis (Henriques et al. 2020, 2021) and to measure exchange (Callaghan and Manz 1994; Callaghan and Furó 2004; Åslund et al. 2009; Lasič et al. 2011; Nilsson et al. 2013; Ning et al. 2018).

The use of DDE to measure the so-called intra-compartmental or microscopic kurtosis, which stems from water molecules reflecting off restricting boundaries, was recently proposed in the correlation tensor imaging (CTI) framework (Henriques et al. 2020, 2021). The approach is based on the cumulant expansion of the DDE signal (Jespersen et al. 2019) and it assumes the long-mixing-time regime where the displacement correlation tensor is proportional to the diffusion covariance tensor (Jespersen et al. 2013; Topgaard 2017) – a relation that allows estimation of isotropic and anisotropic kurtosis (Szczepankiewicz et al. 2015; Westin et al. 2016; Henriques et al. 2020). In practice, the microscopic kurtosis is obtained by subtracting the anisotropic and isotropic kurtoses

from the total kurtosis. Notably, the information used to estimate microscopic kurtosis in CTI is the contrast between an SDE and a parallel DDE acquisition with the same total b-value (Henriques et al. 2021).

Exchange measurement using DDE with variable mixing times has been done in conjunction with both spectroscopy (Callaghan and Furó 2004; Åslund et al. 2009) and imaging (Lasič et al. 2011; Nilsson et al. 2013; Lampinen et al. 2017). In so-called filter-exchange imaging (FEXI) the first pair of diffusion-sensitising gradients (the filter block) is used to suppress the contribution of fast-diffusing water to the measured signal, leading to a decrease in the ADC (Lasič et al. 2011; Nilsson et al. 2013). The return to equilibrium is tracked by measuring the ADC as a function of the mixing time, and the rate of this equilibration is called the apparent exchange rate (AXR). More recent work has unified all experimental designs for probing exchange with dMRI by defining for a given gradient waveform an “exchange sensitivity” (Ning et al. 2018; Chakwizira et al. 2022). This metric is derived assuming multi-Gaussian diffusion and slow-to-intermediate exchange rates. Here, we refer to this framework as multi-Gaussian exchange (MGE), wherein the highest sensitivity to exchange is obtained by contrasting SDE and (parallel) DDE acquisitions with the same b-value.

Evidently, CTI and MGE offer different interpretations of the contrast between SDE and parallel DDE acquisitions at a fixed b-value: the former attributes it to microscopic kurtosis and the latter to exchange. One may suggest that this is because both microscopic kurtosis and exchange arise from the same underlying mechanism, yet this notion is at odds with the physical meaning of both quantities. This work had two aims. First, to reconcile CTI and MGE by developing theory accounting for both microscopic kurtosis and exchange. This is achieved by first extending the previous MGE theory to account for exchange in the presence of anisotropy, enabling the simultaneous estimation of isotropic and anisotropic kurtosis sources as well as exchange. The extended MGE theory also incorporates persistent exchange-independent kurtosis sources that may result from residual voxel anisotropy or powder averaging. Microscopic kurtosis is then introduced as an additional exchange-independent kurtosis source. What enables separation of microscopic kurtosis from exchange in this framework is the distinct signatures that the two processes have on the signal with varying mixing time: exchange causes a dependence on mixing time while microscopic kurtosis (in the long mixing time regime)

does not. The second aim was to investigate the discrepancy between CTI and MGE by performing Monte-Carlo simulations in systems with varying levels of exchange, aiming to pinpoint how estimates of the microscopic kurtosis from CTI and the exchange rate from MGE respond to variations in the underlying microstructure. We demonstrate that exchange and microscopic kurtosis are separate mechanisms and show that the unified approach described above (μ MGE) can disentangle them.

2 Theory

The cumulant expansion

The diffusion-weighted MRI signal can be expressed as the Laplace transform of the spin phase distribution (Price 2009; Callaghan 2011)

$$E = S/S_0 = \int P(\varphi) d\varphi = \langle \exp(-i\varphi) \rangle, \quad (1)$$

where the averaging is done over all contributing spins, E is the normalized signal, S_0 is the non-diffusion-weighted signal and φ is the phase defined through the spin trajectory $\mathbf{r}(t)$ and the diffusion-encoding gradient waveform $\mathbf{g}(t)$ as

$$\varphi = \gamma \int_0^T \mathbf{g}(t) \cdot \mathbf{r}(t) dt, \quad (2)$$

where γ is the gyromagnetic ratio and T is the total duration of $\mathbf{g}(t)$. Equation 1 can be approximated by taking its cumulant expansion

$$\ln(E) \approx -\frac{1}{2} \langle \varphi^2 \rangle + \frac{1}{24} (\langle \varphi^4 \rangle - 3 \langle \varphi^2 \rangle^2) = -\frac{1}{2} c_2 + \frac{1}{24} c_4, \quad (3)$$

where c_2 and c_4 are the second and fourth cumulants of the distribution of φ . In heterogenous media comprising multiple local environments with distinct diffusion properties, averaging must be performed both over spins in each environment and over the environments themselves. Let o_2 and o_4 denote the environment-specific second and fourth cumulants. It can be shown that (Jespersen et al. 2019; Nilsson et al. 2020; Chakwizira et al. 2022)

$$c_2 = \langle o_2 \rangle_e \quad (4)$$

and

$$c_4 = \langle o_4 \rangle_e + 3(\langle o_2^2 \rangle_e - \langle o_2 \rangle_e^2) \quad (5)$$

where the subscript “e” denotes averaging over environments. The first term of Eq. 5 captures the intra-compartmental or microscopic variance (or kurtosis if c_4 is normalized by c_2^2) while the second term is the inter-compartmental variance which may incorporate both isotropic and anisotropic components. Note that theory predicts that $\langle o_4 \rangle_e$ is zero for Gaussian diffusion and negative for restricted diffusion (Jensen et al. 2005). That it is negative for restricted diffusion can be easily understood by considering the signal-versus-b curve of such an environment. For low b-values, it exhibits a mono-exponential attenuation in line with the Gaussian phase approximation (Stepišnik 1993; Vangelder et al. 1994). At higher b-values, it declines more rapidly as the famous diffraction pattern of restricted samples begins to form (Callaghan et al. 1991; Torres et al. 1998; Ozarslan and Basser 2007). This super-exponential attenuation yields negative kurtosis.

CTI

Correlation tensor imaging leverages a combination of SDE, parallel DDE and orthogonal DDE measurements in the long-mixing-time regime to resolve three components of c_4 : isotropic, anisotropic, and microscopic kurtosis (Henriques et al. 2020, 2021). Assuming powder-averaging (Jespersen et al. 2013; Lasič et al. 2014), also known as spherical averaging (Kaden et al. 2016), Eq. 3 evaluates in CTI to

$$\begin{aligned} \ln(\bar{E}_{DDE}(b_1, b_2, \theta)) \\ \approx -(b_1 + b_2)\bar{D} + \frac{1}{6}(b_1^2 + b_2^2)\bar{D}^2 K_T + \frac{1}{2}b_1 b_2 \cos^2(\theta) \bar{D}^2 K_A \\ + \frac{1}{6}b_1 b_2 \bar{D}^2 (2K_I - K_A), \end{aligned} \quad (6)$$

where b_1 and b_2 are the b-values of the first and second gradient pairs, θ is the angle between the two pairs, \bar{D} is the mean diffusivity, K_T is the total kurtosis which is a sum of isotropic (K_I), anisotropic (K_A) and microscopic (K_μ) contributions, such that

$$K_\mu = K_T - K_I - K_A. \quad (7)$$

Note that K_μ is negative in the presence of restricted diffusion, in alignment with expectations of negative kurtosis in restricted compartments (Jensen et al. 2005; Henriques et al. 2020).

An alternative representation can be obtained by defining distinct quantities that are sensitive to the different kurtosis components. To begin with, the shape of the encoding b-tensor can be defined as (Eriksson et al. 2015; Westin et al. 2016)

$$b_\Delta^2 = \frac{b_1^2 + b_2^2 + b_1 b_2 (3 \cos^2 \theta - 1)}{(b_1 + b_2)^2} = \begin{cases} 1; & \text{SDE or parallel DDE} \\ \frac{1}{4}; & \text{orthogonal DDE} \end{cases} \quad (8)$$

Furthermore, we define a new metric that reports on how sensitive the encoding is to the microscopic kurtosis, following the same notion as above, according to

$$b_\mu^2 = \frac{b_1^2 + b_2^2}{(b_1 + b_2)^2} = \begin{cases} 1; & \text{SDE} \\ \frac{1}{2}; & \text{DDE} \end{cases} \quad (9)$$

Using these metrics, we can now rewrite the central CTI equation according to

$$\ln \left(\bar{E}_{DDE}(b, b_\Delta^2, b_\mu^2) \right) = -b\bar{D} + \frac{1}{6} b^2 \bar{D}^2 (K_I + b_\Delta^2 K_A + b_\mu^2 K_\mu) \quad (10)$$

where $b = b_1 + b_2$. Thus, in the CTI framework, sensitivity to K_A is obtained by contrasting parallel and orthogonal DDE measurements, namely

$$\ln \left(\bar{E}_{DDE} \left(b, 1, \frac{1}{2} \right) \right) - \ln \left(\bar{E}_{DDE} \left(b, \frac{1}{4}, \frac{1}{2} \right) \right) = \frac{1}{8} b^2 \bar{D}^2 K_A \quad (11)$$

and sensitivity to K_μ is obtained by contrasting SDE and parallel DDE measurements

$$\ln \left(\bar{E}_{DDE}(b, 1, 1) \right) - \ln \left(\bar{E}_{DDE} \left(b, 1, \frac{1}{2} \right) \right) = \frac{1}{12} b^2 \bar{D}^2 K_\mu \quad (12)$$

The microscopic kurtosis assumes measurements in the long mixing time limit, where K_μ is insensitive to the mixing time, and where the displacement correlation tensor becomes proportional to the diffusion covariance tensor. The long mixing time limit is signified by a vanishing difference between parallel and antiparallel DDE signals.

MGE in one dimension

The one-dimensional multi-Gaussian exchange framework (1D-MGE) assumes negligible intra-compartmental kurtosis but incorporates exchange between Gaussian environments. In 1D-MGE, Eq. 3 for powder-averaged DDE signals (\bar{E}_{DDE}) evaluates to the following signal representation (Ning et al. 2018)

$$\ln(\bar{E}_{DDE}(b, h(k))) \approx -b\bar{D} + \frac{1}{6}b^2\bar{D}^2K_T h(k), \quad (13)$$

where k is the intercompartmental exchange rate and $h(k)$ is the exchange-weighting function given by

$$h(k) = 2 \int_0^T \tilde{q}_4(t) \exp(-kt) dt, \quad (14)$$

where $\tilde{q}_4(t) = q_4(t)/b^2$ and $q_4(t)$ is the fourth-order autocorrelation function of the dephasing q-vector given by $q_4(t) = \int_0^T q^2(t')q^2(t' + t)dt'$. This approach assumes the diffusional heterogeneity of a system to be described by K_T and its homogenization by $h(k)$. Waveforms are more sensitive to exchange when they feature strong phase-dispersion power (q^2) separated in time, as exchange means that, with time, the diffusivity becomes less correlated, which decreases the observed heterogeneity, $K_T h(k)$. From this perspective, exchange is seen as a homogenization of diffusivities.

For small values of kt such that $\exp(-kt) \approx 1 - kt$, $h(k)$ can be written

$$h(k) \approx 1 - k\Gamma, \quad (15)$$

where

$$\Gamma = 2 \int_0^T t \tilde{q}_4(t) dt. \quad (16)$$

is the exchange-weighting time. For SDE with short pulses, Γ is given by

$$\Gamma_{SDE} = \frac{1}{3}\Delta \quad (17)$$

and correspondingly for short-pulse DDE, as

$$\Gamma_{DDE}(b_1, b_2, \Delta, t_m) = \frac{b_1^2 + b_2^2}{3(b_1 + b_2)^2} \Delta + \frac{2b_1 b_2}{(b_1 + b_2)^2} (\Delta + t_m), \quad (18)$$

where Δ is the pulse spacing and t_m is the mixing time. Expressions for the exchange weighting time for acquisitions with finite pulse widths can be found in (Ning et al. 2018).

Notably, sensitivity to the exchange rate in 1D-MGE is obtained by contrasting SDE and parallel DDE signals at a fixed b-value

$$\ln(\bar{E}_{DDE}(b, h_{SDE})) - \ln(\bar{E}_{DDE}(b, h_{DDE})) = \frac{1}{12} b^2 \bar{D}^2 K_T k \left(\frac{2}{3} \Delta + t_m \right) \quad (19)$$

The 1D-MGE framework assumes effects of restricted diffusion can be neglected. Acquisition protocols can be designed to support such an assumption, by featuring waveforms with identical sensitivity to restricted diffusion (Chakwizira et al. 2022). The DDE-based filter exchange imaging (FEXI) approach is an example of such a protocol. When the influence of spoilers cannot be neglected the assumption of equal sensitivity to restricted diffusion is violated (Lasič et al. 2018), but adjustments can be performed to the overall timing of the sequence to address this (Lasic et al. 2024).

Comparing 1D-MGE and CTI

The contrast between SDE and parallel DDE at a fixed b-value is associated with different processes in CTI and 1D-MGE: microscopic kurtosis in the former and exchange in the latter. To better understand the implications of this observation, we equate the right-hand-sides of equations 12 and 19 to obtain

$$\frac{1}{12} b^2 \bar{D}^2 K_\mu = \frac{1}{12} b^2 \bar{D}^2 K_T k \left(\frac{2}{3} \Delta + t_m \right) \quad (20)$$

Equivalently,

$$K_\mu = \left(\frac{2}{3} \Delta + t_m \right) K_T k \quad (21)$$

Equation 21 suggests that in systems that are well-described by multi-Gaussian exchange, CTI will detect this as a non-zero K_μ . Equivalently, in such systems, K_μ estimated with CTI is expected to increase with the underlying exchange rate. Furthermore, in the presence

of exchange, K_μ estimated with CTI is expected to increase with the mixing time. Conversely, in systems with high K_μ , 1D-MGE may detect a high exchange rate even in the absence of exchange. In this work, Monte Carlo simulations will be used to simulate different types of microstructures to understand how these mechanisms may bias results of studies using CTI or 1D-MGE.

Extending 1D-MGE to account for anisotropy and exchange-independent kurtosis

The one-dimensional MGE theory presented in previous sections is well-suited to describing exchange in simple systems with isotropic diffusion, but not where anisotropy is present. We here seek to extend the theory to account for two conditions: (1) exchange in the presence of anisotropy and (2) exchange in pair-wise exchanging components where the pairs themselves are not in exchange. The latter condition can arise from either a system comprising such pair-wise connected components or from acquiring signals in multiple directions in a system with one or more anisotropic exchanging component. This condition gives rise to a "long-time" covariance that persists independent of local exchange.

We begin by generalizing Eq. 13 to account for anisotropy, which necessitates a tensorial description according to

$$\ln E \approx -\mathbf{B} : \mathbf{D} + \frac{1}{2} \mathbf{B}^{\otimes 2}(k) : \mathbb{C}, \quad (22)$$

where

$$\mathbf{B} = \gamma^2 \int_0^T \mathbf{q}^{\otimes 2}(t) dt \quad (23)$$

with

$$\mathbf{q}(t) = \gamma \int_0^t \mathbf{g}(t') dt' \quad (24)$$

is the b-tensor (Westin et al. 2016), " \otimes " denotes outer tensor product, ":" denotes inner product, and $\mathbf{B}^{\otimes 2}(k)$ is the exchange-sensitised "square of the b-tensor", defined as

$$\mathbf{B}^{\otimes 2}(k) = 2 \int_0^T \mathbb{Q}_4(t) \exp(-kt) dt, \quad (25)$$

where $\mathbb{Q}_4(t)$ is the fourth-order autocorrelation tensor of the dephasing \mathbf{q} -vector given by

$$\mathbb{Q}_4(t) = \int_0^T \mathbf{q}^{\otimes 2}(t') \otimes \mathbf{q}^{\otimes 2}(t' + t) dt'. \quad (26)$$

Note that $\mathbf{B}^{\otimes 2}(k)$ becomes more anisotropic with increasing exchange rate. For example, for DDE acquisitions, as the exchange rate grows, the isotropic component of $\mathbf{B}^{\otimes 2}(k)$ converges towards the anisotropic one (cf. Fig 5A). This in itself is an interesting theoretical result, that explains some confusion concerning the use of filter-exchange imaging in systems with anisotropy (see section 7.1 of the supplementary material for details). Finally, \mathbf{D} and \mathbb{C} denote the average diffusion tensor and diffusion-tensor covariance of the local system in exchange (Westin et al. 2016).

In the presence of multiple local systems in exchange, for example in a voxel with multiple fiber orientations, we need an additional term. Recall that Eq. 4 and 5 state that the globally averaged second cumulant is simply the average of the local second cumulants, while the fourth cumulant has contributions both from the average of the local fourth cumulants, as well as the dispersion between second cumulants. Accordingly, the signal representation is given by

$$\ln E \approx -\mathbf{B} : \langle \mathbf{D} \rangle + \frac{1}{2} \langle \mathbf{B}^{\otimes 2}(k) : \mathbb{C} \rangle + \frac{1}{2} \mathbf{B}^{\otimes 2} : \mathbb{C}^\infty, \quad (27)$$

where $\langle \mathbf{D} \rangle$ is the globally averaged diffusion tensor, \mathbb{C}^∞ is the long-time covariance across non-exchanging ensembles that persists despite the presence of local exchange (captured by the first term of Eq. 5), given by $\mathbb{C}^\infty = \langle \mathbf{D}^{\otimes 2} \rangle - \langle \mathbf{D} \rangle^{\otimes 2}$. Thus, as time approaches infinity in the presence of exchange, \mathbb{C}^∞ is the only remaining source of diffusional variance.

Assuming all exchanging systems share the same exchange rate, that is $\langle \mathbf{B}^{\otimes 2}(k) : \mathbb{C} \rangle = \mathbf{B}^{\otimes 2}(k) : \langle \mathbb{C} \rangle$, the powder-average of Eq. 27 is given by

$$\ln E \approx -bD + \frac{1}{2}b^2(k)[V_I + b_\Delta^2(k)V_A] + \frac{1}{2}b^2[V_I^\infty + b_\Delta^2V_A^\infty] \quad (28)$$

where $b = \text{Tr}(\mathbf{B})$ is the trace of b-tensor, $b^2(k)$ and $b_\Delta^2(k)$ are the isotropic and anisotropic projections of $\mathbf{B}^{\otimes 2}(k)$ given by

$$b^2(k) = \mathbf{B}^{\otimes 2}(k) : 9 \mathbb{I}_I \quad (29)$$

and

$$b_\Delta^2(k) = \left(\mathbf{B}^{\otimes 2}(k) : \frac{9}{2} \mathbb{I}_A \right) / b^2(k), \quad (30)$$

where \mathbb{I}_I and \mathbb{I}_A are fourth-order isotropic tensors capturing isotropic and anisotropic variance, respectively (Basser and Pajevic 2003; Eriksson et al. 2015; Westin et al. 2016; Nilsson et al. 2020), $D = \text{Tr}(\mathbf{D})$ is the trace of the average diffusion tensor, V_I and V_A are isotropic and anisotropic variances and V_I^∞ and V_A^∞ are the long-time isotropic and anisotropic variances, respectively.

In terms of kurtosis, Eq. 26 can be written

$$\ln E \approx -bD + \frac{1}{6}b^2(k)D^2[K_I + b_\Delta^2(k)K_A] + \frac{1}{6}b^2[K_I^\infty + b_\Delta^2K_A^\infty] \quad (31)$$

We refer to Eq. 31 as MGE. The kurtosis contributions K_I^∞ can be non-zero due to heterogeneity in isotropic diffusivity between the different systems in exchange, and K_A^∞ can be non-zero for example due to residual voxel anisotropy or powder averaging, as described earlier. Note, however, that this signal representation is degenerate in the absence of exchange ($k = 0$) because $b^2(0) = b^2$ and $b_\Delta^2(0) = b_\Delta^2$ and thus there is no way of separating K_I^∞ from K_I or K_A from K_A^∞ .

Reconciling CTI and MGE

It appears that CTI and MGE have competing interpretations of the contrast between SDE and DDE at a fixed diffusion-weighting, as the previous sections highlighted. Alternatively, the two approaches can be viewed as complimentary, each describing different features of the diffusion process. Here, we propose and explore a unification of the two approaches that could possibly enable simultaneous estimation of both the exchange rate and microscopic kurtosis. We achieve this by introducing microscopic kurtosis into the MGE theory as an additional component of the total kurtosis that is exchange-independent but is not accounted for by K_I^∞ and K_A^∞ . This results in the unified signal representation which we refer to as μMGE , given by

$$\ln E \approx -bD + \frac{1}{6}b^2(k)D^2[K_I + b_\Delta^2(k)K_A] + \frac{1}{6}b^2[K_I^\infty + b_\Delta^2K_A^\infty + b_\mu^2K_\mu] \quad (32)$$

where b_μ^2 is as defined earlier. Note that while MGE can be applied to experiments with arbitrary gradient waveforms, μMGE is restricted to DDE setups with fixed timing parameters but variable mixing times, due to the assumptions in CTI and the definition of b_μ^2 . Note that CTI and the 1D-MGE theory presented earlier are both special cases of this unified approach.

3 Methods

Protocol design

Synthetic signals were generated using three different acquisition protocols. All three protocols used gradient strengths typical of preclinical systems. The first protocol was designed as described in (Henriques et al. 2021). The protocol comprised four sets of acquisitions with different combinations of b_1 , b_2 and θ (Fig. 1A and B). Set 1 had $b_1 = 2.5$ ms/ μm^2 , $b_2 = 0$ and 45 rotations chosen to minimise electrostatic repulsion on a sphere. Set 2 had $b_1 = b_2 = 1.25$ ms/ μm^2 , $\theta = 0^\circ$ and rotated as in Set 1. Set 3 had $b_1 = b_2 = 1.25$ ms/ μm^2 , $\theta = 90^\circ$, rotated as in Set 1. The acquisition was repeated for three equidistant

directions of the second gradient pair, yielding in total 135 rotations for Set 3. Set 4 had $b_1 = b_2 = 0.5 \text{ ms}/\mu\text{m}^2$, $\theta = 0^\circ$ and rotated as in Set 1. Pulse timing parameters were $\delta = 3.5 \text{ ms}$ and $\Delta = t_m = 12 \text{ ms}$.

A second protocol was designed to verify the fulfilment of the long-mixing-time regime required for CTI. This protocol featured the same general timing settings, but only two gradient waveforms designed to yield $(b_1, b_2, \theta) = (0.5 \text{ ms}/\mu\text{m}^2, 0.5 \text{ ms}/\mu\text{m}^2, 0^\circ)$ and $(b_1, b_2, \theta) = (0.5 \text{ ms}/\mu\text{m}^2, 0.5 \text{ ms}/\mu\text{m}^2, 180^\circ)$.

Finally, a third protocol was created to assess the effects of a variable mixing time on CTI K_μ estimates and to evaluate MGE (Eq. 31) and μMGE (Eq. 32). This protocol was identical to the first one, except that it featured five mixing times for both parallel and orthogonal DDE (12, 25, 50, 75 and 100 ms) and six b-values for both SDE and DDE acquisitions (0.25, 0.5, 1, 1.5, 2 and $2.5 \text{ ms}/\mu\text{m}^2$).

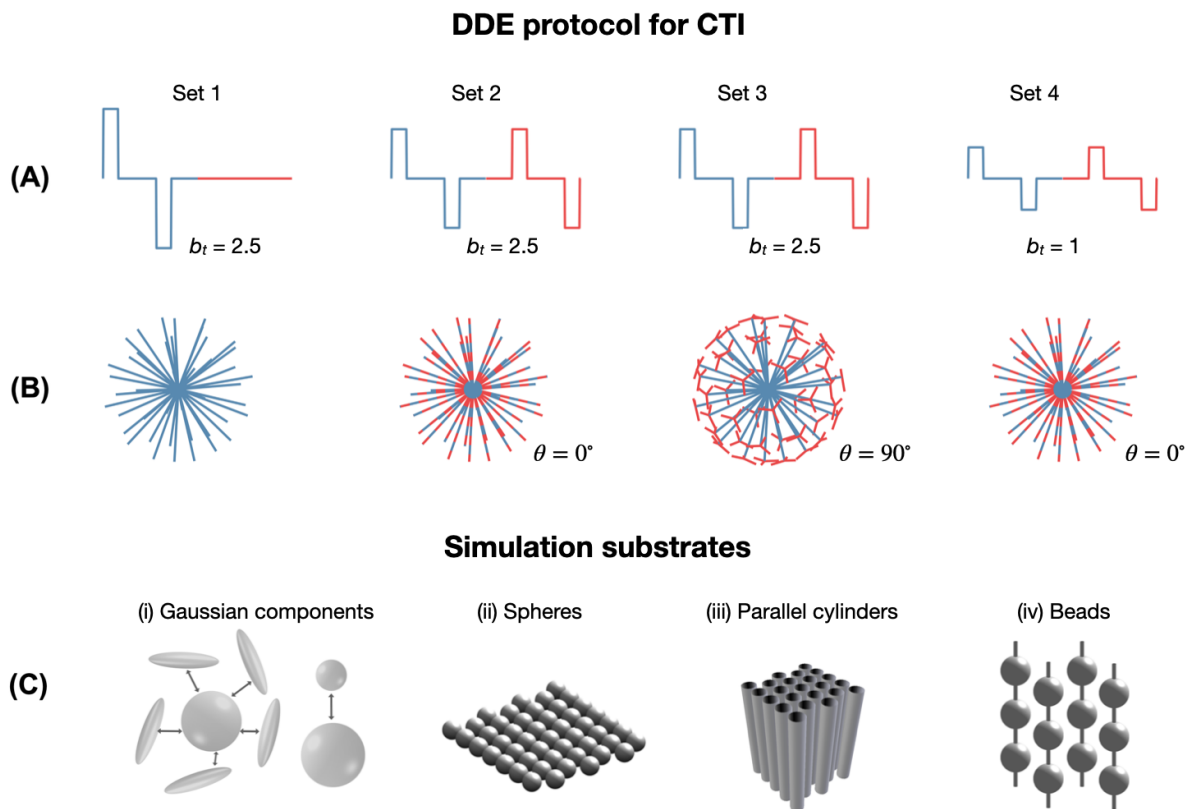


Figure 1: Protocols and substrates used in simulations. (A) shows four sets of DDE waveforms with different combinations of b-values b_1 and b_2 , $b_t = b_1 + b_2$ denotes the total b-values and θ is the angle

between the first and second gradient pairs. (B) shows the rotation schemes used in each acquisition set. Set 1 has $(b_1, b_2, \theta) = (2.5, 0, 0^\circ)$ rotated in 45 directions chosen to minimise electrostatic repulsion on a sphere. Set 2 has $(b_1, b_2, \theta) = (1.25, 1.25, 0^\circ)$ rotated as in set 1. Set 3 has $(b_1, b_2, \theta) = (1.25, 1.25, 90^\circ)$ rotated as in set 1 and repeated for three equidistant directions of the second gradient pair. Set 4 has $(b_1, b_2, \theta) = (0.5, 0.5, 0^\circ)$ rotated as in set 1. Panel (C) shows the four simulation substrates used: sets of isotropic and anisotropic Gaussian components in exchange with each other, regularly packed spheres of diameter $6\ \mu\text{m}$, regularly packed parallel cylinders of diameter $6\ \mu\text{m}$ and beading structures with maximum and minimum diameters of $6\ \mu\text{m}$ and $1\ \mu\text{m}$.

Microstructure simulations

In order to investigate exchange-induced bias in CTI-estimated microscopic kurtosis and to evaluate the removal of such bias by the μMGE approach, Monte Carlo simulations were performed in three different substrates: regularly packed spheres of diameter $6\ \mu\text{m}$ (packing density = 50%), regularly packed cylinders of diameter $6\ \mu\text{m}$ (packing density = 75%) and beading structures with minimum and maximum diameters of 1 and $6\ \mu\text{m}$ (packing density = 40%), all in exchange with the extracellular space (Fig. 1C). Barrier permeability was varied to yield exchange rates between 0 and $50\ \text{s}^{-1}$. Other simulation parameters were: number of particles = 10^6 , temporal resolution = $0.5\ \mu\text{s}$, bulk diffusivity = $2\ \mu\text{m}^2/\text{ms}$ and intra- and extracellular particle populations were initialised to maintain equal particle densities in each compartment. In each simulation scenario, signals were generated using the protocols described in the preceding section. The simulations were executed using an inhouse-written GPU-accelerated simulation framework (<https://github.com/arthur-chakwizira/Pasidi>, c.f. supplementary material of (Chakwizira et al. 2022)).

Gaussian simulations

While the microstructure simulations described above are more realistic than simulations of purely Gaussian diffusion, they lack a known ground truth microscopic kurtosis and potentially feature restriction-induced diffusion time-dependence which is not accounted for by any of the theories considered in this work. For this reason, Monte Carlo simulations were also performed in Gaussian components featuring either isotropic-to-isotropic exchange (“iso-iso Gaussian”) or isotropic-to-anisotropic exchange

(“iso-aniso Gaussian”) (Fig. 1C). In both cases, the ground truth microscopic kurtosis was known (zero). These simulations used the same number of particles and temporal resolution as the microstructure simulations but featured two pools with diffusion tensors given by $[D_{iso}, D_{\Delta}] = [2 \mu\text{m}^2/\text{ms}, 0]$ and $[0.5 \mu\text{m}^2/\text{ms}, 0]$ for the “iso-iso” case and $[D_{iso}, D_{\Delta}] = [0.5, 1]$ and $[1.5 \mu\text{m}^2/\text{ms}, 0]$ for the “iso-aniso” case. The anisotropic tensor was oriented along the x-direction. Pool fractions were set to 0.5 in each case. The same simulation framework that was used for the microstructure simulations was also used for the Gaussian case.

Analytical simulations

The μMGE theory contains many free parameters. It is thus relevant to determine whether all parameters could be estimated from noisy signals. This was achieved by studying the dependence of the coefficients of K_I , K_A and K_{μ} in Eq. 32 on mixing time and exchange rate. The rationale was that any correlation between these coefficients would result in an underdetermined equation system which makes it challenging to disentangle the parameters they encode for. For this part of the study, the exchange rate was varied from 0 to 200 s^{-1} . The second part of the feasibility study involved generating signals with the μMGE signal representation for different combinations of exchange rate and microscopic kurtosis, corrupting the signals with Rice-distributed noise at $\text{SNR} = 200$ and fitting μMGE to those signals. Two sets of simulations were performed. In the first K_{μ} was varied between 0 and 1 at exchange rates of 10, 30 and 50 s^{-1} . In the second, the exchange rate was varied between 10 and 50 s^{-1} at K_{μ} -values of 0, 0.5 and 1. In both simulations, K_I and K_A were both set to 1, and K_I^{∞} and K_A^{∞} were both set to 0.5.

Data analysis

Signals simulated using the protocols and substrates in Fig. 1 were powder-averaged and CTI parameter estimates were obtained by fitting Eq. 10. Fulfilment of the long-mixing-time condition was checked by computing the difference between the log of powder-averaged signals obtained with the parallel and antiparallel DDE protocols. 1D-MGE parameter estimates were obtained by fitting Eq. 13 to a subset of the powder-averaged

data with $\theta = 0^\circ$. MGE (Eq. 31) was evaluated using signals generated with the extended protocol (featuring multiple mixing times and b-values) in substrates of spheres, iso-iso Gaussian and iso-aniso Gaussian. The signals were corrupted with Rice-distributed noise at a generous SNR of 200 prior to fitting. Numerical evaluation of μ MGE was done by fitting Eq. 32 to signals generated using the extended protocol in all substrates shown in Fig. 1 using exchange rates between 5 and 50 s⁻¹. In each case, μ MGE kurtosis estimates were compared to the CTI kurtosis estimates under the same simulation settings.

Throughout this study, fitting was performed using the method *lsqnonlin* in MATLAB (The MathWorks, Natick, MA, R2022a). All fitting code and the simulated signals can be found in the repository at <https://github.com/arthur-chakwizira/cti-mge>.

4 Results

Figure 2 shows the powder-averaged CTI signals in four different simulation substrates using the protocols shown in Fig. 1. Corresponding estimates of K_T , K_I , K_A and K_μ are shown alongside the signals. Results are shown in the absence of exchange (column A) and in the presence of fast exchange at a rate of 50 s⁻¹ (column B). In the absence of exchange, there is a small positive K_μ in the substrates of spheres, cylinders and beads. The Gaussian case gives zero K_μ , as expected. In the presence of exchange, there is a large positive K_μ in all substrates. The observed isotropic and anisotropic kurtosis decrease with the introduction of exchange. Note that the same analysis applied to substrate of spheres with only intra-cellular particles yields a negative microscopic kurtosis, in alignment with expectations (c.f Fig. A1 of the supplementary material). Note, however, that intracellular simulations in the substrate of beads gave a large positive microscopic kurtosis (Fig. A1).

The parallel-antiparallel log signal difference was 0.0007, 0.0002 and 0.0004 for the substrates of spheres, beads and cylinders, at a mixing time of 12 ms, which are all close to zero, indicating that the long-mixing time regime was attained.

The dependence of CTI-estimated K_μ on the underlying exchange rate and on the mixing time is shown in Fig. 3, for the substrates of spheres of diameter 6 μ m and isotropic

exchanging Gaussian components. K_μ from CTI grows with the underlying exchange rate and with the mixing time when exchange is non-zero, in accordance with the prediction of Eq. 21. Figure 3 also shows estimates of the exchange rate obtained with 1D-MGE (Eq. 13), which are independent of the mixing time and correlate strongly with the ground truth. This indicates that the substrate of exchanging spheres is well-approximated by the multi-Gaussian assumption.

Figure 4 shows MGE parameter estimates in exchanging Gaussian components that are either isotropic or anisotropic. Kurtosis estimates are largely independent of the underlying exchange rate and agree well with the ground truth, especially for faster exchange. Exchange rate estimates obtained with MGE correlate well with the ground truth, with a slight bias attributable to the influence of higher order terms in the cumulant expansion. Similar results were obtained in the substrate of spheres and are shown in Fig. A2 of the supplementary material. Note that the long-time kurtosis parameters display a more pronounced exchange-rate dependence with decreasing exchange rate, illustrating the innate degeneracy of Eq. 31 at slow exchange. The behaviour of the estimates as the exchange rate approaches zero is shown in Fig. A3 of the supplementary material.

Figure 5 shows the results of studying the feasibility of estimating the parameters of the μ MGE model (Eq. 32) under different simulation settings. The encoding coefficients shown in panel A indicate that at zero exchange rate, it is not possible to disentangle the isotropic and anisotropic kurtoses from their long-time variants. At intermediate exchange rates, all parameters of the representation can be estimated unambiguously. At very high exchange rates, the mixing time dependence is again lost for all coefficients and the remaining contrast is only between SDE and DDE. This makes it difficult to disentangle microscopic kurtosis from very fast exchange. Panel B of Fig. 5 shows the parameter estimates obtained by fitting Eq. 32 to noisy signals generated using the same equation. Estimates in all scenarios agree with the ground truth, indicating the feasibility of estimating the parameters of the μ MGE model for non-zero exchange rates. Note that these simulations were performed with the analytical model, and only report on the ability to solve the inverse problem. They do not report on the applicability of the model to any specific type of microstructure.

Figure 6 shows CTI and μ MGE parameter estimates in four substrates: permeable spheres, permeable beads and exchanging Gaussian components with either isotropic or anisotropic diffusion. In all substrates, CTI kurtosis estimates depend on the exchange rate. Fitting μ MGE removes this dependence and allows simultaneous estimation of microscopic kurtosis and the exchange rate. Exchange estimates obtained with μ MGE correlate well with the ground truth. The performance of μ MGE in cylinders was poorer, however. This result is presented in Fig. A4 of the supplementary material.

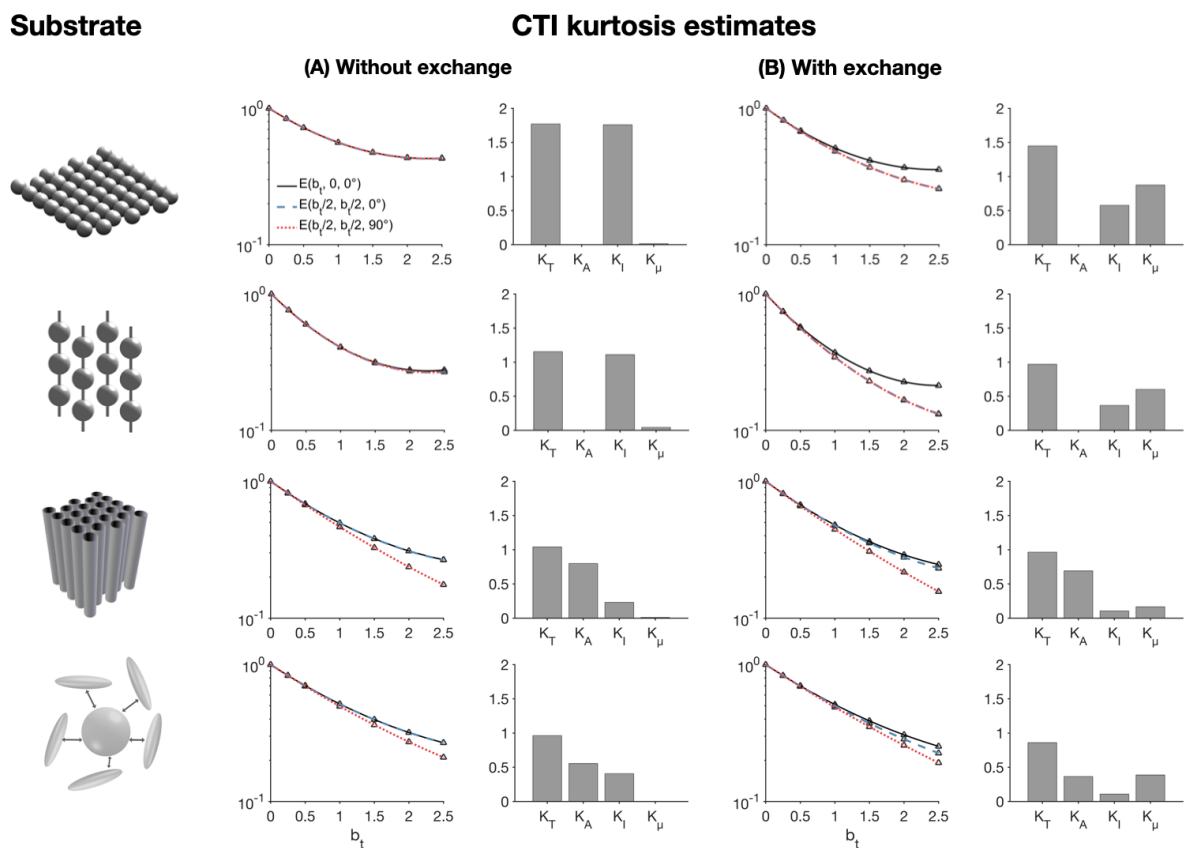


Figure 2: CTI simulated signals and parameter estimates. The first column shows the simulation substrates used for generation of each of results in (A) and (B). (A) shows powder-averaged signals obtained with the CTI protocol in Fig. 1 for the case of zero exchange. Corresponding CTI estimates of total, isotropic, anisotropic and microscopic kurtosis are shown alongside the signals. The same results are presented in (B) but in the presence of exchange at a rate of 50 s^{-1} . Microscopic kurtosis is small in all substrates in (A) but increases notably when exchange is introduced in (B). Note that microscopic kurtosis is not expected to increase with exchange according to the CTI framework.

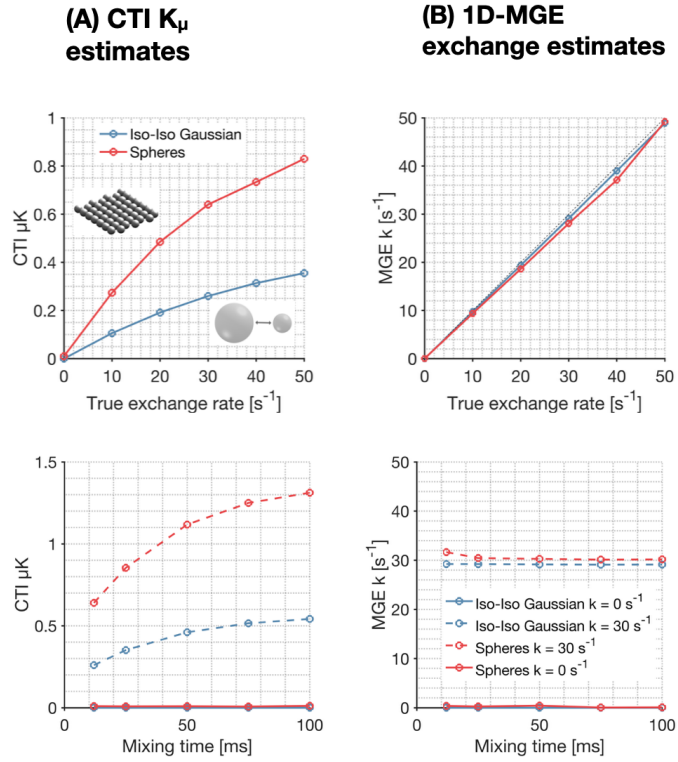


Figure 3: Variation of microscopic kurtosis with exchange rate and mixing time. Exchange estimates from 1D-MGE are shown alongside for comparison. Results are shown in substrates of regular spheres in exchange with the extracellular space and isotropic Gaussian components in exchange. In both substrates, CTI-estimated microscopic kurtosis increases with the true exchange rate and the mixing time (A) when exchange is non-zero, in line with the prediction of Eq. 21. Note that the dependence on mixing time and exchange rate disappears at very fast exchange or very long mixing times. Exchange estimates obtained with 1D-MGE, on the contrary, show an independence on mixing time (B) and correlate well with the ground truth.

MGE kurtosis and exchange estimates

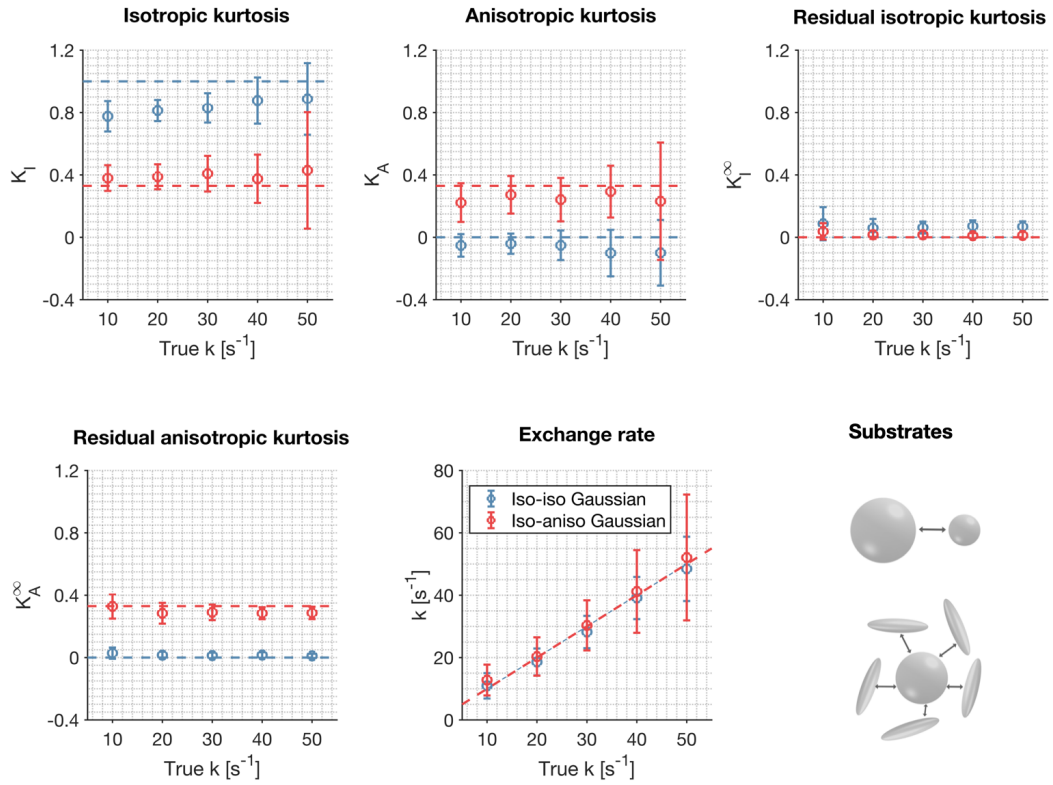


Figure 4: Evaluation of MGE in different substrates: isotropic Gaussian components in exchange (Iso-Iso Gaussian) and anisotropic Gaussian components in exchange with an isotropic component (Iso-Aniso Gaussian). Estimates were obtained from signals generated at an SNR of 200. The kurtosis estimates show – as expected – a weak to no dependence on the true exchange rate. MGE exchange estimates in all three substrates agree well with the ground truth.

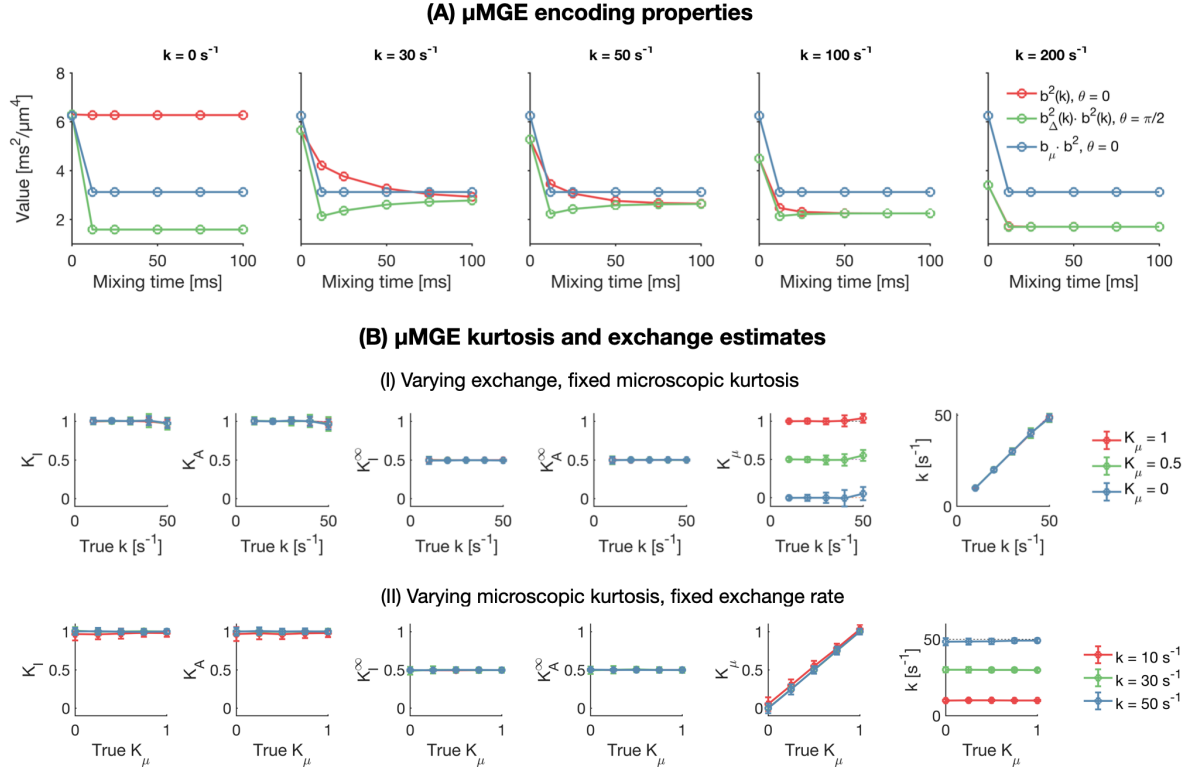


Figure 5: Study of the invertibility of the μ MGE representation. (A) shows the dependence of the coefficients of K_I , K_A , and K_μ in Eq. 30 on mixing time for different exchange rates. The lack of dependence on mixing time of the coefficients of K_I and K_A , at zero exchange rate means that these parameters cannot be disentangled from their long-time variants K_I^∞ and K_A^∞ . At intermediate exchange rates, all parameters of Eq. 30 can be estimated from the signals. At very fast exchange ($k = 200$ /s), the dependence on mixing time is again lost, making it difficult to disentangle the exchange rate from microscopic kurtosis. Panel B shows parameter estimates obtained by generating signals using the μ MGE representation (Eq. 30), corrupting the signals with Rice-distributed noise at SNR = 200 and fitting the same equation to those signals. Row (I) shows kurtosis and exchange estimates for a fixed microscopic kurtosis and varying exchange rate. Row (II) shows the same estimates for a fixed exchange rate and varying microscopic kurtosis. In all settings, the parameter estimates agree with the ground truth values, indicating that the μ MGE signal representation is invertible at non-zero exchange rates.

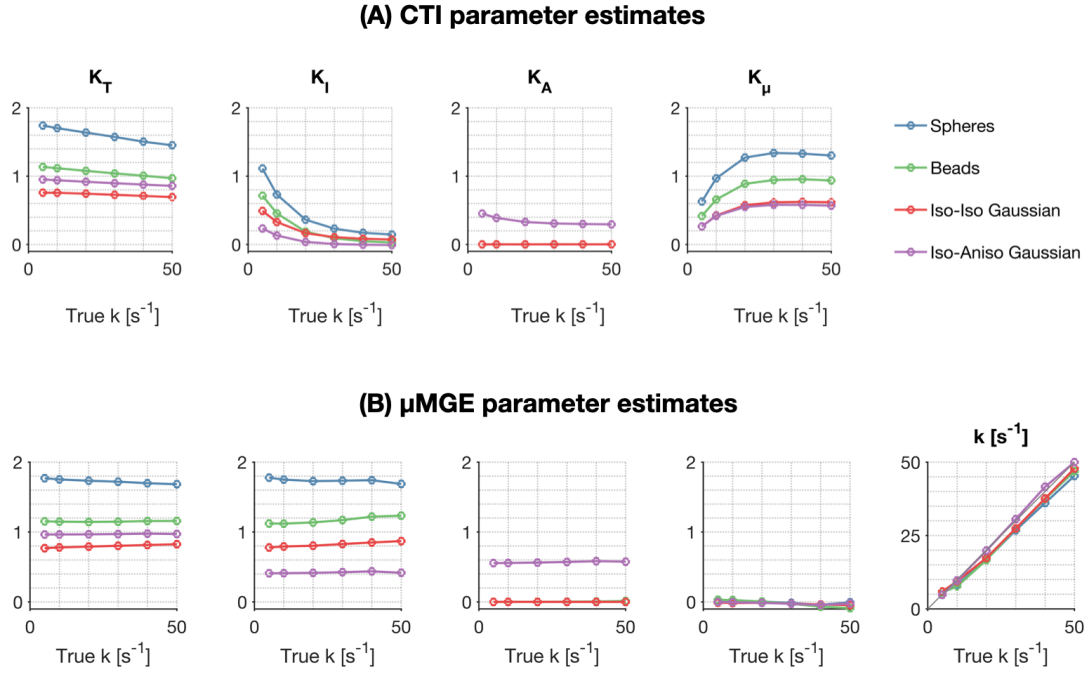


Figure 6: Evaluation of the μ MGE representation in different substrates. Results are shown for noiseless signals generated in spheres in exchange with the extracellular space, beads in exchange with the extracellular space, exchanging isotropic Gaussian components and anisotropic Gaussian components in exchange with isotropic. All CTI kurtosis estimates vary with the exchange rate. μ MGE kurtosis estimates are – as expected – largely independent of the exchange rate in all substrates. μ MGE exchange estimates agree well with the ground truth.

5 Discussion

This study has shown using both theory and simulations (Eq. 21, Fig. 2-3) that microscopic kurtosis estimated with CTI is positively biased by exchange and that exchange estimates obtained with the 1D-MGE theory can be positively biased by microscopic kurtosis. Importantly, in the presence of exchange, CTI-estimated microscopic kurtosis depends on the mixing time (Fig. 3), whereas the exchange rate as estimated by 1D-MGE is invariant to the mixing time. Furthermore, we extend the 1D-MGE theory to account for anisotropy and residual time-independent kurtosis components and validate it with simulations (Fig. 4). Microscopic kurtosis is then introduced into the MGE signal representation, forming the μ MGE approach, and simulations indicate that it can disentangle exchange from microscopic kurtosis (Fig. 6). While this approach could in principle be applied in future work to simultaneously map

microscopic kurtosis and exchange, it is a demanding experimental approach. This begs the question of whether new studies based on data acquired with DDE should apply CTI, 1D-MGE, MGE, or μ MGE in their data analysis. The answer depends on the situation, and we will provide perspectives to inform the decision.

Exchange estimation with diffusion MRI has garnered increasing interest in recent years. Several studies have applied FEXI to map the AXR in the healthy human brain (Nilsson et al. 2013; Lampinen et al. 2017; Bai et al. 2020), brain tumours (Lampinen et al. 2017), breast cancer (Lasič et al. 2016) and in animal models on preclinical scanners (Sønderby et al. 2014; Li et al. 2023). Recent work has also shown sensitivity of the AXR parameter to blood-brain-barrier exchange (Powell et al. 2023). Other studies have applied diffusion-exchange spectroscopy (DEXSY) to measure relatively high AXR in the ex-vivo mouse brain (Williamson et al. 2020; Cai et al. 2022). A new class of models based on a combination of the standard model and the Kärger model has been recently developed and applied to map exchange in the rat brain using SDE with variable diffusion times (Jelescu et al. 2022; Olesen et al. 2022). More recent work has demonstrated the utility of free gradient waveforms for mapping exchange in the human brain unconfounded by restricted diffusion (Chakwizira et al. 2022, 2023). The general consensus regarding exchange in the brain is that it is negligible between the intra- and extra-axonal spaces in white matter at clinically-accessible diffusion times and this finding is explained by the presence of myelin sheaths (Badaut et al. 2011; Bai et al. 2018; Brusini et al. 2019; Veraart et al. 2019; Jelescu et al. 2020). In ischemic brain tissue, exchange times between approximately 50 and 500 ms have been reported (Lätt et al. 2009; Lampinen et al. 2021). Gray matter is more complicated. The powder-averaged signal at strong diffusion weighting deviates from the typical inverse-square-root dependence on the b-value characteristic of impermeable sticks which indicates non-negligible exchange between neurites and the extracellular space or neurites and soma (Jelescu et al. 2020; Veraart et al. 2020; Olesen et al. 2022). Exchange estimates in gray matter are, nonetheless, still largely inconsistent, with literature values ranging from 4 ms to hundreds of milliseconds (Jelescu et al. 2020; Olesen et al. 2022). The theory (Eq. 21) predicts that non-zero microscopic kurtosis manifests as exchange even in the absence of exchange. Without additional experiments with multiple mixing times, it is difficult to assess the degree to which these results were biased by microscopic kurtosis.

CTI is a novel technique that leverages dedicated DDE experiments to probe the displacement correlation tensor containing information about isotropic and anisotropic kurtosis (Henriques et al. 2020, 2021). A subtraction of the isotropic and anisotropic components from the total kurtosis provides the microscopic kurtosis—a kurtosis component assumed to be zero in previous approaches based on the multi-Gaussian diffusion assumption (Szczepankiewicz et al. 2015; Westin et al. 2016; Henriques et al. 2020, 2021). Simulations previously used to validate CTI were based on an ad hoc introduction of microscopic kurtosis via an analytical signal decay (Henriques et al. 2021) and are thus difficult to compare to the present work that performs Monte Carlo simulations designed to mimic a realistic dMRI experiment of tissue with water in both intra- and extracellular spaces. It is worth noting, however, that the supplementary material of (Henriques et al. 2021) reports results of Monte Carlo simulations inside spheres where the estimated negative K_μ (approximately -0.4) is in good agreement with our estimates (Fig. A1). More recent work validates CTI using Monte Carlo simulations inside beading structures with varying beading amplitudes (Alves et al. 2022) where large positive K_μ (approximately 5) was observed in the substrate with the highest degree of beading. A large positive K_μ inside beading structures is consistent with the findings of the present work (Fig. A1) and may in fact be explained by the presence of exchange between the wider and narrower regions of the beading structure. Moreover, Alves et al. (Alves et al. 2022) report separately on K_μ estimates from the intracellular and extracellular spaces of the beading structures, where the latter shows K_μ close to zero. Including both intracellular and extracellular signals in the estimation of K_μ resulted in negligible K_μ given a typical bulk diffusivity of $2 \mu\text{m}^2/\text{ms}$ —also in agreement with the present work. Since its conception, CTI has been applied in various conditions. For example, K_μ was mapped in healthy volunteers where it appeared larger in cortical grey matter than in white matter (Novello et al. 2022). In a mouse model of stroke lesions, a large increase in K_μ (between 50 and 100%) was observed in the ischemic regions and the authors attribute this increase to higher cell cross-sectional variance or restricted diffusion (Alves et al. 2022). In summary, values of K_μ of up to 0.5 were reported in the healthy human brain and up to about 1 in stroke lesions, both of which are higher than what the present study detects in simulations featuring both intra- and extracellular signals. On this note, we would like to raise awareness that—as shown throughout this

work (Figs. 2,3,6)— K_μ can be biased by the presence of exchange. The observations of elevated K_μ in grey matter and stroke lesions are *consistent* with previous reports of fast exchange in these tissues (Lätt et al. 2009; Lampinen et al. 2021; Chakwizira et al. 2023) and thus the reported values of K_μ may reflect exchange. To empirically distinguish between exchange and microscopic kurtosis, we advocate for an acquisition protocol featuring at least two mixing times for parallel DDE acquisitions. Exchange causes a signal dependence on mixing time while microscopic kurtosis does not.

Both exchange and microscopic kurtosis can influence the signal, and therefore the reliable and unambiguous estimation of both effects is valuable. This work presents a first step in that direction (Eq. 32) by unifying the MGE theory with the concept of microscopic kurtosis from CTI into the μ MGE model. Simulations showed that the signal representation is invertible at intermediate exchange rates (Fig. 5) and disentangles microscopic kurtosis from exchange in a variety of simulation substrates (Fig. 6). This approach may provide a good candidate for an analysis framework in cases where both exchange and microscopic kurtosis are expected to be relevant, such as in grey matter (Novello et al. 2022; Chakwizira et al. 2023). However, as highlighted earlier, the theory has an innate degeneracy at zero exchange rate (Fig. A3), but the minimum exchange rate that can be estimated can be reduced by designing a protocol with longer mixing times. The approach could also benefit from post-hoc tests of whether the estimation of all parameters is supported by the data, using for example Bayesian information criteria, Akaike's information criterion (Foesleitner et al. 2022), or the F-test (Lampinen et al. 2020). The theory also showed poorer performance in the substrate of cylinders (Fig. A4), a finding attributable to unmodelled time-dependence effects from restricted/hindered diffusion outside the cylinders (Burcaw et al. 2015; Lee et al. 2018). According to the restriction-exchange framework of Chakwizira et al. (Chakwizira et al. 2022), the DDE protocol considered in this work should have minimal influence from restricted diffusion as the waveforms have fixed restriction weighting. However, this is only true to first order and for diffusion perpendicular to the cylinder axis. Another explanation may be the influence of higher-order terms which impacts all analysis frameworks that are based on the cumulant expansion (Kiselev 2010; Chuhutin et al. 2017; Nilsson et al. 2020). A rigorous protocol optimisation to minimise the influence of the effects described above is reserved for future work.

The apparent directional dependence of exchange in anisotropic systems is known. S nderby et al. (S nderby et al. 2014) applied FEXI in multiple directions in both a yeast phantom and perfusion-fixated monkey brain and found that AXR was rotationally invariant in the yeast phantom but direction-dependent in anisotropic regions of the monkey brain. A theoretical study by Lasic et al. (Lasic et al. 2016) revealed that AXR becomes anisotropic even in environments with a single exchange rate when there are more than two orientationally dispersed components. Li et al. (Li et al. 2022) applied FEXI in multiple directions in human white matter and found that the AXR perpendicular to the fiber orientation was significantly larger than the AXR parallel to it. A simulation study by Ludwig et al. (Ludwig et al. 2021) showed that at least 30 gradient directions were required to reliably estimate AXR in the presence of orientation dispersion. We have for the first time presented an exchange theory that explicitly takes anisotropy into account, by uniting concepts from the previous 1D-MGE theory (Ning et al. 2018) and the b-tensor encoding framework (Szczepankiewicz et al. 2015; Westin et al. 2016). Numerical simulations in both isotropic and anisotropic substrates (Fig. 4) indicate that the new theory correctly captures the exchange rate even in the presence of anisotropy. Another noteworthy aspect of the theory is the incorporation of residual time-independent kurtosis that may result from powder averaging or the presence of non-exchanging compartments in a voxel. This kurtosis component has been described in previous work (Lee et al. 2020; Zhang et al. 2021; Li et al. 2023) and the present work has illustrated its relevance with numerical simulations (Fig. 4).

In conclusion, this work has demonstrated that exchange can confound the estimation of microscopic kurtosis and vice versa. We have presented and numerically evaluated new exchange theory accounting for anisotropy and allowing simultaneous and unambiguous estimation of both microscopic kurtosis and exchange. We challenge the notion of microscopic kurtosis and exchange being two sides of the same coin and propose the view of them as two separate phenomena that are distinguishable with appropriate modeling and experimental design.

6 References

- Aggarwal M, Smith MD, Calabresi PA. Diffusion-time dependence of diffusional kurtosis in the mouse brain. *Magn Reson Med*. 2020 Sep;84(3):1564–78.
- Albers GW. Expanding the window for thrombolytic therapy in acute stroke. The potential role of acute MRI for patient selection. *Stroke*. 1999 Oct;30(10):2230–7.
- Alexander DC, Dyrby TB, Nilsson M, Zhang H. Imaging brain microstructure with diffusion MRI: practicality and applications. *NMR in Biomedicine*. 2019;32(4):e3841.
- Alves R, Henriques RN, Kerkelä L, Chavarrías C, Jespersen SN, Shemesh N. Correlation Tensor MRI deciphers underlying kurtosis sources in stroke. *NeuroImage*. 2022 Feb 15;247:118833.
- Åslund I, Nowacka A, Nilsson M, Topgaard D. Filter-exchange PGSE NMR determination of cell membrane permeability. *Journal of Magnetic Resonance*. 2009 Oct 1;200(2):291–5.
- Assaf Y, Blumenfeld-Katzir T, Yovel Y, Basser PJ. Axcaliber: A method for measuring axon diameter distribution from diffusion MRI. *Magnetic Resonance in Medicine*. 2008;59(6):1347–54.
- Badaut J, Ashwal S, Adami A, Tone B, Recker R, Spagnoli D, et al. Brain water mobility decreases after astrocytic aquaporin-4 inhibition using RNA interference. *J Cereb Blood Flow Metab*. 2011 Mar;31(3):819–31.
- Bai R, Li Z, Sun C, Hsu YC, Liang H, Basser P. Feasibility of filter-exchange imaging (FEXI) in measuring different exchange processes in human brain. *NeuroImage*. 2020 Oct 1;219:117039.
- Bai R, Springer Jr. CS, Plenz D, Basser PJ. Fast, Na^+/K^+ pump driven, steady-state transcytolemmal water exchange in neuronal tissue: A study of rat brain cortical cultures. *Magnetic Resonance in Medicine*. 2018;79(6):3207–17.
- Basser PJ, Mattiello J, LeBihan D. MR diffusion tensor spectroscopy and imaging. *Biophys J*. 1994 Jan;66(1):259–67.
- Basser PJ, Pajevic S. A normal distribution for tensor-valued random variables: applications to diffusion tensor MRI. *IEEE Transactions on Medical Imaging*. 2003 Jul;22(7):785–94.
- Brabec J, Friedjungová M, Vašata D, Englund E, Bengzon J, Knutsson L, et al. Meningioma microstructure assessed by diffusion MRI: An investigation of the source of mean diffusivity and fractional anisotropy by quantitative histology. *Neuroimage Clin*. 2023 Mar 2;37:103365.
- Brusini L, Menegaz G, Nilsson M. Monte Carlo Simulations of Water Exchange Through Myelin Wraps: Implications for Diffusion MRI. *IEEE Trans Med Imaging*. 2019 Jun;38(6):1438–45.

- Burcaw LM, Fieremans E, Novikov DS. Mesoscopic structure of neuronal tracts from time-dependent diffusion. *NeuroImage*. 2015 Jul 1;114:18–37.
- Cai TX, Williamson NH, Ravin R, Basser PJ. Disentangling the effects of restriction and exchange with diffusion exchange spectroscopy. *Front Phys*. 2022;10:805793.
- Callaghan P, Manz B. *Velocity Exchange Spectroscopy*. 1994;
- Callaghan PT. *Translational Dynamics and Magnetic Resonance: Principles of Pulsed Gradient Spin Echo NMR*. OUP Oxford; 2011.
- Callaghan PT, Coy A, MacGowan D, Packer KJ, Zelaya FO. Diffraction-like effects in NMR diffusion studies of fluids in porous solids. *Nature*. 1991 Jun;351(6326):467–9.
- Callaghan PT, Eccles CD, Xia Y. NMR microscopy of dynamic displacements: k-space and q-space imaging. *J Phys E: Sci Instrum*. 1988 Aug;21(8):820.
- Callaghan PT, Furó I. Diffusion-diffusion correlation and exchange as a signature for local order and dynamics. *J Chem Phys*. 2004 Feb 22;120(8):4032–8.
- Callaghan PT, Komlosh ME. Locally anisotropic motion in a macroscopically isotropic system: displacement correlations measured using double pulsed gradient spin-echo NMR. *Magnetic Resonance in Chemistry*. 2002;40(13):S15–9.
- Callaghan PT, Xia Y. Velocity and diffusion imaging in dynamic NMR microscopy. *Journal of Magnetic Resonance (1969)*. 1991 Feb 1;91(2):326–52.
- Caprihan A, Fukushima E. Flow measurements by NMR. *Physics Reports*. 1990 Dec 1;198(4):195–235.
- Chakwizira A, Westin CF, Brabec J, Lasič S, Knutsson L, Szczepankiewicz F, et al. Diffusion MRI with pulsed and free gradient waveforms: Effects of restricted diffusion and exchange. *NMR in Biomedicine*. 2022;n/a(n/a):e4827.
- Chakwizira A, Zhu A, Foo T, Westin CF, Szczepankiewicz F, Nilsson M. Diffusion MRI with free gradient waveforms on a high-performance gradient system: Probing restriction and exchange in the human brain [Internet]. *arXiv*; 2023 [cited 2023 Jun 1]. Available from: <http://arxiv.org/abs/2304.02764>
- Chen Y, Zhao X, Ni H, Feng J, Ding H, Qi H, et al. Parametric mapping of brain tissues from diffusion kurtosis tensor. *Comput Math Methods Med*. 2012;2012:820847.
- Chenevert TL, Stegman LD, Taylor JM, Robertson PL, Greenberg HS, Rehemtulla A, et al. Diffusion magnetic resonance imaging: an early surrogate marker of therapeutic efficacy in brain tumors. *J Natl Cancer Inst*. 2000 Dec 20;92(24):2029–36.
- Chuhutin A, Hansen B, Jespersen SN. Precision and accuracy of diffusion kurtosis estimation and the influence of b-value selection. *NMR in Biomedicine*. 2017;30(11):e3777.
- Cory DG, Garroway AN, Miller JB. Applications of spin transport as a probe of local geometry. In 1990. p. 149–50.

- Drake-Pérez M, Boto J, Fittsiori A, Lovblad K, Vargas MI. Clinical applications of diffusion weighted imaging in neuroradiology. *Insights Imaging*. 2018 Aug;9(4):535–47.
- Eriksson S, Lasič S, Nilsson M, Westin CF, Topgaard D. NMR diffusion-encoding with axial symmetry and variable anisotropy: Distinguishing between prolate and oblate microscopic diffusion tensors with unknown orientation distribution. *J Chem Phys*. 2015 Mar 14;142(10):104201.
- Fieremans E, Burcaw LM, Lee HH, Lemberskiy G, Veraart J, Novikov DS. In vivo observation and biophysical interpretation of time-dependent diffusion in human white matter. *NeuroImage*. 2016 Apr 1;129:414–27.
- Fieremans E, Jensen JH, Helpert JA. White matter characterization with diffusional kurtosis imaging. *Neuroimage*. 2011 Sep 1;58(1):177–88.
- Foesleitner O, Sulaj A, Sturm V, Kronlage M, Godel T, Preisner F, et al. Diffusion MRI in Peripheral Nerves: Optimized b Values and the Role of Non-Gaussian Diffusion. *Radiology*. 2022 Jan;302(1):153–61.
- Henriques RN, Jespersen SN, Shemesh N. Correlation tensor magnetic resonance imaging. *NeuroImage*. 2020 May 1;211:116605.
- Henriques RN, Jespersen SN, Shemesh N. Evidence for microscopic kurtosis in neural tissue revealed by correlation tensor MRI. *Magnetic Resonance in Medicine*. 2021;86(6):3111–30.
- Jelescu IO, Palombo M, Bagnato F, Schilling KG. Challenges for biophysical modeling of microstructure. *Journal of Neuroscience Methods*. 2020 Oct 1;344:108861.
- Jelescu IO, de Skowronski A, Geffroy F, Palombo M, Novikov DS. Neurite Exchange Imaging (NEXI): A minimal model of diffusion in gray matter with inter-compartment water exchange. *NeuroImage*. 2022 Aug 1;256:119277.
- Jensen JH, Helpert JA, Ramani A, Lu H, Kaczynski K. Diffusional kurtosis imaging: The quantification of non-gaussian water diffusion by means of magnetic resonance imaging. *Magnetic Resonance in Medicine*. 2005;53(6):1432–40.
- Jespersen SN, Lundell H, Sønderby CK, Dyrby TB. Orientationally invariant metrics of apparent compartment eccentricity from double pulsed field gradient diffusion experiments. *NMR in Biomedicine*. 2013;26(12):1647–62.
- Jespersen SN, Olesen JL, Ianaş A, Shemesh N. Effects of nongaussian diffusion on “isotropic diffusion” measurements: An ex-vivo microimaging and simulation study. *Journal of Magnetic Resonance*. 2019 Mar 1;300:84–94.
- Kaden E, Kruggel F, Alexander DC. Quantitative mapping of the per-axon diffusion coefficients in brain white matter. *Magn Reson Med*. 2016 Apr;75(4):1752–63.
- Kiselev V. The Cumulant Expansion: An Overarching Mathematical Framework For Understanding Diffusion NMR. In 2010.

- Koch MA, Finsterbusch J. Towards compartment size estimation in vivo based on double wave vector diffusion weighting. *NMR Biomed.* 2011 Dec;24(10):1422–32.
- Lampinen B, Lätt J, Wasselius J, Westen D van, Nilsson M. Time dependence in diffusion MRI predicts tissue outcome in ischemic stroke patients. *Magnetic Resonance in Medicine.* 2021;86(2):754–64.
- Lampinen B, Szczepankiewicz F, Lätt J, Knutsson L, Mårtensson J, Björkman-Burtscher IM, et al. Probing brain tissue microstructure with MRI: principles, challenges, and the role of multidimensional diffusion-relaxation encoding. *NeuroImage.* 2023 Aug 19;120338.
- Lampinen B, Szczepankiewicz F, Mårtensson J, van Westen D, Hansson O, Westin CF, et al. Towards unconstrained compartment modeling in white matter using diffusion-relaxation MRI with tensor-valued diffusion encoding. *Magnetic Resonance in Medicine.* 2020;84(3):1605–23.
- Lampinen B, Szczepankiewicz F, van Westen D, Englund E, C Sundgren P, Lätt J, et al. Optimal experimental design for filter exchange imaging: Apparent exchange rate measurements in the healthy brain and in intracranial tumors. *Magn Reson Med.* 2017 Mar;77(3):1104–14.
- Lasic S, Chakwizira A, Lundell H, Westin CF, Nilsson M. Tuned Exchange Imaging (TEXI) – A modified Filter-Exchange Imaging pulse sequence for applications with thin slices and restricted diffusion. *Proceedings of ISMRM Singapore.* 2024;
- Lasic S, Jespersen SN, Lundell H, Nilsson M, Dyrby TB, Topgaard D. Apparent Exchange Rate in Multi-compartment Anisotropic Tissue. *Proceedings of the ISMRM Singapore.* 2016;
- Lasič S, Lundell H, Topgaard D, Dyrby TB. Effects of imaging gradients in sequences with varying longitudinal storage time—Case of diffusion exchange imaging. *Magnetic Resonance in Medicine.* 2018;79(4):2228–35.
- Lasič S, Nilsson M, Lätt J, Ståhlberg F, Topgaard D. Apparent exchange rate mapping with diffusion MRI. *Magnetic Resonance in Medicine.* 2011;66(2):356–65.
- Lasič S, Oredsson S, Partridge SC, Saal LH, Topgaard D, Nilsson M, et al. Apparent exchange rate for breast cancer characterization. *NMR in Biomedicine.* 2016;29(5):631–9.
- Lasič S, Szczepankiewicz F, Eriksson S, Nilsson M, Topgaard D. Microanisotropy imaging: quantification of microscopic diffusion anisotropy and orientational order parameter by diffusion MRI with magic-angle spinning of the q-vector. *Front Phys [Internet].* 2014 [cited 2021 Jul 10];2. Available from: <https://www.frontiersin.org/articles/10.3389/fphy.2014.00011/full>
- Lätt J, Nilsson M, van Westen D, Wirestam R, Ståhlberg F, Brockstedt S. Diffusion-weighted MRI measurements on stroke patients reveal water-exchange mechanisms in sub-acute ischaemic lesions. *NMR in Biomedicine.* 2009;22(6):619–28.

- Le Bihan D. Diffusion MRI: what water tells us about the brain. *EMBO Mol Med*. 2014 May;6(5):569–73.
- Lee HH, Fieremans E, Novikov DS. What dominates the time dependence of diffusion transverse to axons: Intra- or extra-axonal water? *Neuroimage*. 2018 Nov 15;182:500–10.
- Lee HH, Papaioannou A, Novikov DS, Fieremans E. In vivo observation and biophysical interpretation of time-dependent diffusion in human cortical gray matter. *Neuroimage*. 2020 Nov 15;222:117054.
- Li C, Fieremans E, Novikov DS, Ge Y, Zhang J. Measuring water exchange on a preclinical MRI system using filter exchange and diffusion time dependent kurtosis imaging. *Magnetic Resonance in Medicine*. 2023;89(4):1441–55.
- Li Z, Pang Z, Cheng J, Hsu YC, Sun Y, Özarslan E, et al. The direction-dependence of apparent water exchange rate in human white matter. *NeuroImage*. 2022 Feb 15;247:118831.
- Ludwig D, Laun FB, Ladd ME, Bachert P, Kuder TA. Apparent exchange rate imaging: On its applicability and the connection to the real exchange rate. *Magnetic Resonance in Medicine*. 2021;86(2):677–92.
- Mitra PP. Multiple wave-vector extensions of the NMR pulsed-field-gradient spin-echo diffusion measurement. *Phys Rev B*. 1995 Jun 1;51(21):15074–8.
- Moseley ME, Cohen Y, Kucharczyk J, Mintorovitch J, Asgari HS, Wendland MF, et al. Diffusion-weighted MR imaging of anisotropic water diffusion in cat central nervous system. *Radiology*. 1990a Aug;176(2):439–45.
- Moseley ME, Kucharczyk J, Mintorovitch J, Cohen Y, Kurhanewicz J, Derugin N, et al. Diffusion-weighted MR imaging of acute stroke: correlation with T2-weighted and magnetic susceptibility-enhanced MR imaging in cats. *AJNR Am J Neuroradiol*. 1990b May;11(3):423–9.
- Nilsson M, Englund E, Szczepankiewicz F, van Westen D, Sundgren PC. Imaging brain tumour microstructure. *Neuroimage*. 2018 Nov 15;182:232–50.
- Nilsson M, Lätt J, Westen D van, Brockstedt S, Lasič S, Ståhlberg F, et al. Noninvasive mapping of water diffusional exchange in the human brain using filter-exchange imaging. *Magnetic Resonance in Medicine*. 2013;69(6):1572–80.
- Nilsson M, Szczepankiewicz F, Brabec J, Taylor M, Westin CF, Golby A, et al. Tensor-valued diffusion MRI in under 3 minutes: an initial survey of microscopic anisotropy and tissue heterogeneity in intracranial tumors. *Magnetic Resonance in Medicine*. 2020;83(2):608–20.
- Ning L, Nilsson M, Lasič S, Westin CF, Rathi Y. Cumulant expansions for measuring water exchange using diffusion MRI. *J Chem Phys*. 2018 Feb 21;148(7):074109.

- Novello L, Henriques RN, İanuş A, Feiweier T, Shemesh N, Jovicich J. In vivo Correlation Tensor MRI reveals microscopic kurtosis in the human brain on a clinical 3T scanner. *NeuroImage*. 2022 Jul 1;254:119137.
- Olesen JL, Østergaard L, Shemesh N, Jespersen SN. Diffusion time dependence, power-law scaling, and exchange in gray matter. *NeuroImage*. 2022 May 1;251:118976.
- Ozarslan E, Basser PJ. MR diffusion - “diffraction” phenomenon in multi-pulse-field-gradient experiments. *J Magn Reson*. 2007 Oct;188(2):285–94.
- Özarslan E, Basser PJ. Microscopic anisotropy revealed by NMR double pulsed field gradient experiments with arbitrary timing parameters. *J Chem Phys*. 2008 Apr 21;128(15):154511.
- Özarslan E, Koay CG, Shepherd TM, Komlosh ME, İrfanoğlu MO, Pierpaoli C, et al. Mean apparent propagator (MAP) MRI: a novel diffusion imaging method for mapping tissue microstructure. *Neuroimage*. 2013 Sep;78:16–32.
- Panagiotaki E, Walker-Samuel S, Siow B, Johnson SP, Rajkumar V, Pedley RB, et al. Noninvasive Quantification of Solid Tumor Microstructure Using VERDICT MRI. *Cancer Res*. 2014 Apr 1;74(7):1902–12.
- Powell E, Ohene Y, Battiston M, Dickie BR, Parkes LM, Parker GJM. Blood-brain barrier water exchange measurements using FEXI: Impact of modeling paradigm and relaxation time effects. *Magnetic Resonance in Medicine*. 2023;90(1):34–50.
- Price WS. NMR Studies of Translational Motion: Principles and Applications [Internet]. Cambridge: Cambridge University Press; 2009 [cited 2023 Jan 5]. (Cambridge Molecular Science). Available from: <https://www.cambridge.org/core/books/nmr-studies-of-translational-motion/0A471425EE21B8F2EC91AF163E98F3F6>
- Reynaud O. Time-Dependent Diffusion MRI in Cancer: Tissue Modeling and Applications. *Front Phys* [Internet]. 2017 [cited 2021 Jun 3];5. Available from: <https://www.frontiersin.org/articles/10.3389/fphy.2017.00058/full>
- Ross BD, Moffat BA, Lawrence TS, Mukherji SK, Gebarski SS, Quint DJ, et al. Evaluation of cancer therapy using diffusion magnetic resonance imaging. *Mol Cancer Ther*. 2003 Jun;2(6):581–7.
- Shemesh N, Jespersen SN, Alexander DC, Cohen Y, Drobnjak I, Dyrby TB, et al. Conventions and nomenclature for double diffusion encoding NMR and MRI. *Magnetic Resonance in Medicine*. 2016;75(1):82–7.
- Shemesh N, Özarslan E, Adiri T, Basser PJ, Cohen Y. Noninvasive bipolar double-pulsed-field-gradient NMR reveals signatures for pore size and shape in polydisperse, randomly oriented, inhomogeneous porous media. *J Chem Phys*. 2010 Jul 28;133(4):044705.
- Sønderby CK, Lundell HM, Søgaaard LV, Dyrby TB. Apparent exchange rate imaging in anisotropic systems. *Magnetic Resonance in Medicine*. 2014;72(3):756–62.

- Stejskal EO, Tanner JE. Spin Diffusion Measurements: Spin Echoes in the Presence of a Time-Dependent Field Gradient. *J Chem Phys.* 1965 Jan 1;42(1):288–92.
- Stepišnik J. Time-dependent self-diffusion by NMR spin-echo. *Physica B: Condensed Matter.* 1993 May 1;183(4):343–50.
- Szczepankiewicz F, Lasič S, van Westen D, Sundgren PC, Englund E, Westin CF, et al. Quantification of microscopic diffusion anisotropy disentangles effects of orientation dispersion from microstructure: applications in healthy volunteers and in brain tumors. *Neuroimage.* 2015 Jan 1;104:241–52.
- Topgaard D. Multidimensional diffusion MRI. *J Magn Reson.* 2017 Feb;275:98–113.
- Torres AM, Michniewicz RJ, Chapman BE, Young GA, Kuchel PW. Characterisation of erythrocyte shapes and sizes by NMR diffusion-diffraction of water: correlations with electron micrographs. *Magn Reson Imaging.* 1998 May;16(4):423–34.
- Tsien C, Cao Y, Chenevert T. Clinical Applications for Diffusion MRI in Radiotherapy. *Semin Radiat Oncol.* 2014 Jul;24(3):218–26.
- Vangelder P, Despres D, Vanzijl PCM, Moonen CTW. Evaluation of Restricted Diffusion in Cylinders. Phosphocreatine in Rabbit Leg Muscle. *Journal of Magnetic Resonance, Series B.* 1994 Mar 1;103(3):255–60.
- Veraart J, Fieremans E, Novikov DS. On the scaling behavior of water diffusion in human brain white matter. *NeuroImage.* 2019 Jan 15;185:379–87.
- Veraart J, Nunes D, Rudrapatna U, Fieremans E, Jones DK, Novikov DS, et al. Noninvasive quantification of axon radii using diffusion MRI. *Elife.* 2020 Feb 12;9:e49855.
- Westin CF, Knutsson H, Pasternak O, Szczepankiewicz F, Özarslan E, van Westen D, et al. Q-space trajectory imaging for multidimensional diffusion MRI of the human brain. *NeuroImage.* 2016 Jul 15;135:345–62.
- Williamson NH, Ravin R, Cai TX, Benjamini D, Falgairolle M, O'Donovan MJ, et al. Real-time measurement of diffusion exchange rate in biological tissue. *J Magn Reson.* 2020 Aug;317:106782.
- Zhang J, Lemberskiy G, Moy L, Fieremans E, Novikov DS, Kim SG. Measurement of cellular-interstitial water exchange time in tumors based on diffusion-time-dependent diffusional kurtosis imaging. *NMR Biomed.* 2021 Jun;34(6):e4496.

7 Appendix

7.1 On the relation between MGE and filter-exchange imaging

A relation between MGE and FEXI can be obtained by deriving the dependence of the ADC on the mixing time, defined according to

$$D'(t_m) = -\frac{1}{b_d} [\ln E_{f+d} - \ln E_d] \quad (\text{A. 1})$$

where E_{f+d} and E_d are the diffusion-weighted signals from acquisitions with the filtering and detection block active and detection only, respectively. These signals can be predicted using the MGE framework. We assume DDE acquisitions with short pulses which allows the exchange-sensitised square of the b-tensor to be written

$$\mathbf{B}^{\otimes 2}(k) = 2 \int_0^T \mathbb{Q}_4(t) \exp(-kt) dt = \mathbb{Q}_4^0 \Delta h_0(k, \Delta) + 2\mathbb{Q}_4^1 \Delta h_1(k, \Delta, t_m) \quad (\text{A. 2})$$

where $\mathbb{Q}_4^0 = \mathbb{Q}_4(0)$ and $\mathbb{Q}_4^1 = \mathbb{Q}_4(t_m + \Delta)$, $h_0(k, \Delta) = \frac{\Delta k + e^{-\Delta k} - 1}{\Delta^2 k^2}$ and

$$h_1(k, \Delta, t_m) = \left[\frac{e^{-t_m k} - e^{-k(\Delta+t_m)} - \Delta k e^{-k(\Delta+t_m)}}{\Delta^2 k^2} \right] + \left[\frac{e^{-kT} + kT e^{-k(\Delta+t_m)} - e^{-k(\Delta+t_m)} - k\Delta e^{-k(\Delta+t_m)} - kt_m e^{-k(\Delta+t_m)}}{\Delta^2 k^2} \right].$$

Assuming $k\Delta \ll 1$ gives $h_0(k, \Delta) \approx 1/2$ and $h_1(k, \Delta, t_m) \approx e^{-kt_m}$. $\mathbf{B}^{\otimes 2}(k)$ can then be written

$$\mathbf{B}^{\otimes 2}(k) = \mathbf{B}_f^{\otimes 2} + \mathbf{B}_d^{\otimes 2} + 2\mathbf{B}_f \otimes \mathbf{B}_d e^{-kt_m} \quad (\text{A. 3})$$

The isotropic and anisotropic projections of $\mathbf{B}^{\otimes 2}(k)$ can then be expressed

$$b_I^2(k) = (b_f^2 + b_d^2) + 2b_f b_d e^{-kt_m} \quad (\text{A. 4})$$

$$b_A^2(k) = (b_f^2 + b_d^2) + 2b'_\Delta b_f b_d e^{-kt_m} \quad (\text{A. 5})$$

where $b'_\Delta = 1$ for SDE and parallel DDE and $b'_\Delta = -\frac{1}{2}$ for orthogonal DDE. For simplicity, we re-write the MGE representation as:

$$\ln E \approx -bD + \frac{1}{2} [b_I^2(k)V_I + b_A^2(k)V_A] \quad (\text{A. 6})$$

Now the desired signal difference is given by

$$D'(t_m) = \langle D \rangle - \frac{1}{2} b_d [V_I + V_A] - \frac{1}{2} b_f e^{-kt_m} [V_I + b'_\Delta V_A] \quad (A.7)$$

At long mixing times, $t_m \rightarrow \infty$, the diffusivity approaches its equilibrium value

$$D^{eq} = \langle D \rangle - \frac{1}{2} b_d [V_I + V_A] \approx \langle D \rangle \quad (A.8)$$

where the approximation assumes b_d is low. Defining the filter efficiency as

$$\sigma = 2b_f \frac{(V_I + b'_\Delta V_A)}{\langle D \rangle} \quad (A.9)$$

gives us the well-known FEXI signal equation:

$$D'(t_m) = D^{eq} [1 - \sigma e^{-kt_m}]. \quad (A.10)$$

Note that Eq. A.9 implies that the filter efficiency for orthogonal DDE can be negative if $V_A > 2 \cdot V_I$.

7.2 Supplementary figures

This section contains CTI kurtosis estimates in substrates of spheres and beads, where the intracellular and extracellular signals were analysed separately. MGE kurtosis and exchange estimates in multi-Gaussian components at slow exchange and in spheres that feature non-Gaussian diffusion with exchange are also presented herein. Finally, CTI and μ MGE are compared in the substrate of parallel cylinders.

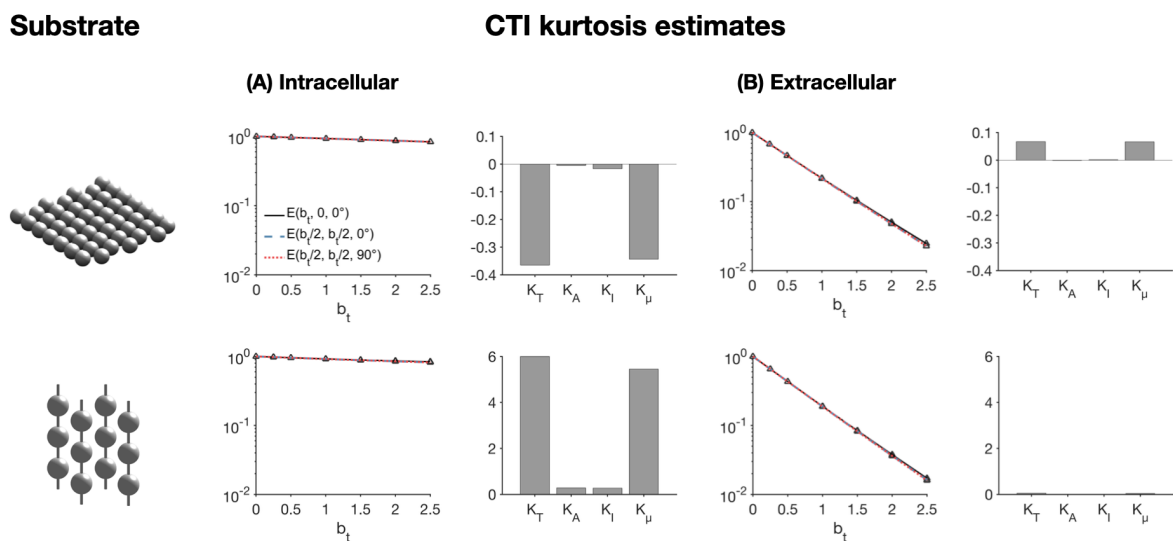


Figure A1: CTI parameter estimates in the substrates of 6 μm -diameter spheres and beads. The estimates were obtained by separately fitting the CTI signal representation to the intracellular and extracellular signals. For cylinders, the intracellular signals give a large negative microscopic kurtosis, while the extracellular space has a small positive microscopic kurtosis. For beads, there is a large positive microscopic kurtosis from the intracellular signals and a very small positive microscopic kurtosis from the extracellular signals.

MGE kurtosis and exchange estimates

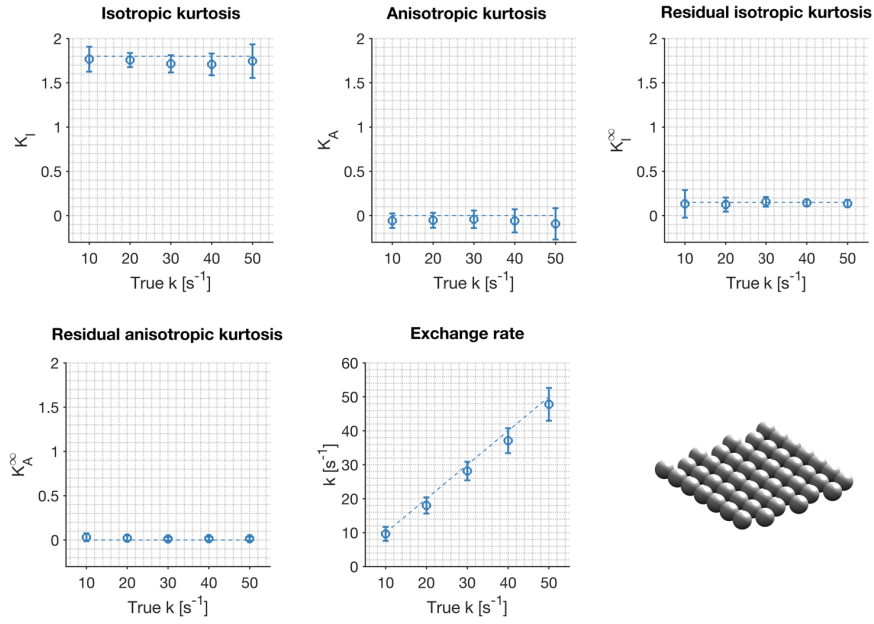


Figure A2: MGE parameter estimates in spheres at SNR = 200. The dashed lines indicate ground truth. The kurtosis is dominated by the isotropic components as expected. All estimates show good agreement with ground truth, with a small bias that can be explained by higher-order effects associated with the cumulant expansion.

MGE kurtosis and exchange estimates at low exchange rates

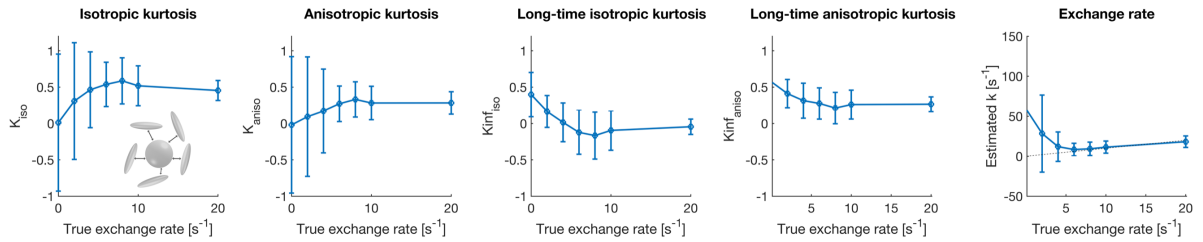


Figure A3: MGE parameter estimates for anisotropic Gaussian components in exchange with an isotropic component. This is the equivalent of Fig. 4 but for lower exchange rates. The dependence on exchange rate of the kurtosis estimates, the bias in estimated exchange rates and the relatively large uncertainties at low exchange rates indicate the difficulty of inverting the MGE signal representation around $k = 0$.

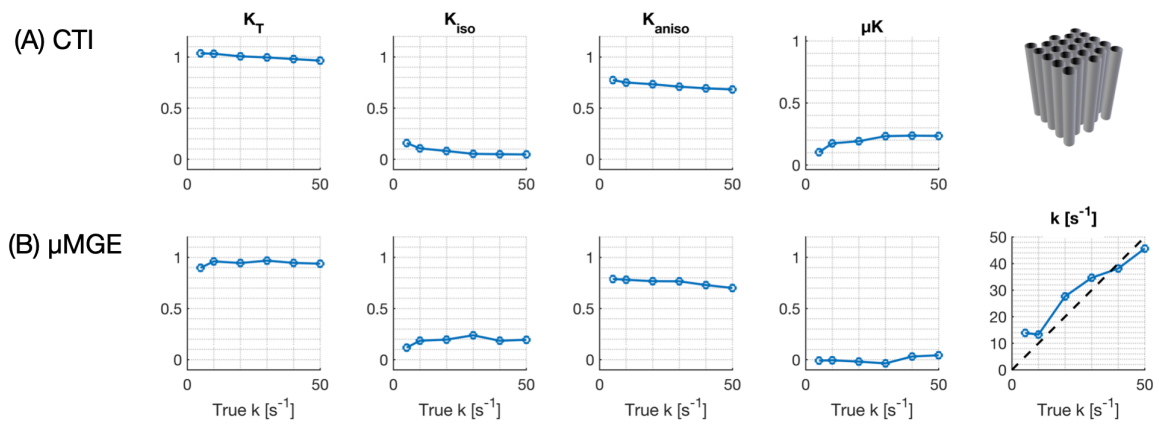


Figure A4: Evaluation of μ MGE in a substrate of parallel cylinders. Fitting μ MGE largely removes the dependence of microscopic kurtosis on exchange rate that is seen with CTI. However, exchange estimates are not as stable as those presented in Fig. 6.